PAPER

Check for updates

Efficient electrocatalyst of α-Fe$_2$O$_3$ nanorings for oxygen evolution reaction in acidic conditions†

Xiaolei Liang,[ab] Jinmei Qian,[b] Yonggang Liu, [ID][b] Zhengmei Zhang[b] and Daqiang Gao [ID] *[b]

Large-scale application of sustainable energy devices urgently requires cost-effective electrocatalysts to overcome the sluggish kinetics related to the oxygen evolution reaction (OER) under acidic conditions. Here, we first report the highly efficient electrocatalytic characteristics of α-Fe$_2$O$_3$ nanorings (NRs), which exhibits prominent OER electrocatalytic activity with lower overpotential of 1.43 V at 10 mA cm^{-2} and great stability in 1 M HCl, surpassing the start-of-the art Ir/C electrocatalyst. The significantly optimized OER activity of the α-Fe$_2$O$_3$ NRs mainly attributes to the synergistic effect of the excellent electrical conductivity and a large effective active surface because of their unique nanoring structure, disordered surface, and the dynamic stability of α-Fe$_2$O$_3$ NRs in acidic conditions.

Introduction

The oxygen evolution reaction (OER) is of great significance to renewable energy storage, conversion and collection systems including water spilling, rechargeable metal–air batteries.[1–3] However, this half-reaction suffers from sluggish kinetics because it requires high overpotential to propel the four-electron process.[4,5] Exploring high-efficiency, low-cost and robust durability electrocatalysts is urgently needed to replace conventional noble-metal materials such as Ir/C and RuO$_2$, as well as further reducing the overpotential and promoting electrocatalytic activity.[6,7] In recent years, 3d transition metal oxides have become promising electrocatalysts because of their unique electronic structure, earth-abundance and sufficient stability.[8–13] Specifically, α-Fe$_2$O$_3$ (hematite) has been widely used in photoelectrochemistry because of its optimal band gap (~0.2 eV), superior corrosion resistance, non-toxicity and abundant resources.[14–17] However, sluggish kinetics seriously affect its further practical applications in electrocatalysis.[18]

In the past few years, great strategies, such as introducing defects, elemental doping, regulating surface orientation, altering nanostructure and combining with other conductive substrate, have been devoted to reducing OER overpotential of electrocatalysts.[15,19–22] Particularly, designing electrocatalysts with specific nanostructures has attracted growing attention as

they own abundant active sites and great stability.[23] Recently, reports indicate the rapid dissolution occurs for metal oxide and perovskite-based electrocatalysts during OER process, which demonstrates that the excellent activity of the electrocatalyst is inversely correlated with its stability.[24–27] Hence, it is also critical to develop OER electrocatalysts with both high performance and dynamically stability. In addition, exploring affordable electrocatalysts for OER at a low pH is urgently needed to develop inexpensive renewable energy systems, because the acidic medium provides a fast start-up time and limited crossover that contributes to the high purity of the electrocatalysts and reduced resistance loss.[28–30]

Based on above considerations, we therefore developed a simple approach to synthesize α-Fe$_2$O$_3$ electrocatalyst with nanorings (NRs) morphology. As our expected, α-Fe$_2$O$_3$ NRs featured excellent OER activity with a lower overpotential and great kinetics, along with outstanding stability in acid electrolyte, much better than that of bulk α-Fe$_2$O$_3$ and commercial Ir/C. This efficient OER electrocatalytic activity of α-Fe$_2$O$_3$ NRs may be related to the unique nanoring structure, where α-Fe$_2$O$_3$ NRs show larger effective electrocatalytic active surface area and increased electrical conductivity than that of bulk one in acidic electrolyte.

Experiment

Synthesis of α-Fe$_2$O$_3$ NRs

Ammonium dihydrogen phosphate (MAP; AR; ≥99.0%), ferric chloride hexahydrate (FeCl$_3$·6H$_2$O; AR; ≥99.0%) were purchased from Sigma-Aldrich. Absolute alcohol was used as received. The α-Fe$_2$O$_3$ NRs were fabricated by a facile hydrothermal method. In brief, after fully mixing 0.5 M FeCl$_3$ aqueous solution, 0.02 M MAP aqueous solution and 38.5 mL DI water,

[a] Key Laboratory for Gynecologic Oncology Gansu Province, Department of Obstetrics and Gynecology, The First Hospital of Lanzhou University, China. E-mail: gaodq@lzu.edu.cn

[b] Key Laboratory for Magnetism and Magnetic Materials of MOE, Key Laboratory of Special Function Materials and Structure Design of MOE, Lanzhou University, Lanzhou 730000, China

transferred to 50 mL Teflon-lined stainless autoclaves and stirred evenly, then sealed and reacted at 220 °C for 48 h. Finally, the resulting products were washed with 1 : 1 volume ration of alcohol and water, and dried thoroughly at 60 °C to obtain the red solid powder. For comparison, the bulk α-Fe₂O₃ was purchased from Aladdin.

Structure characterization

In order to investigate the structure, morphology, and Fe valence states of α-Fe₂O₃ NRs and bulk one, we use X-ray diffraction (XRD) on Philips/X'Pert Pro diffractometer with Cu Kα radiation, scanning/transmission electron microscopy (SEM/TEM) on Hitachi S-4800 and Tecnai G2 F30, FEI devices, as well as X-ray photoelectron spectroscopy (XPS) on Kratos Axis Ultra system, respectively. Besides, the synchrotron source of Beijing was used to measure Fe K-edge X-ray absorption near-edge spectroscopy (XANES) and extended X-ray absorption fine structure (EXAFS). In addition, the valence states of Fe were also evaluated by Mössbauer spectroscopy on Wissel (Germany).

Electrochemical OER test

All of the electrocatalytic OER tests were carried out on a CHI660E work station at room temperature under acidic conditions (1 M HCl), where Ag/AgCl and carbon rod were selected as reference/counter electrode. To the working electrode (the electrode area is 0.071 cm^{-2}), 5 mg catalyst and 5 mg carbon black (Vulcan XC72) were dispersed in 50 mL petroleum ether. Then the 6 mg dried powder, 30 μL Nafion-117 solution with 1470 μL DMF were added into 5 mL container and ultra-sonication for 2 h. Afterward, the 18 μg fresh ink electrocatalyst of (carbon black and Fe₂O₃ materials) was pipetted onto the stationary glassy carbon electrode with 0.25 mg cm^{-2}. Meanwhile, in order to collect more electrocatalyst to measure XRD, XPS, TEM and EXAFS of cycled α-Fe₂O₃ NRs, the fresh ink electrocatalyst was pipetted onto carbon cloth (1 cm × 2 cm) with 0.25 mg cm^{2} to conduct OER CV cycling, LSV and i–t curve. And the linear sweep voltammetry curves were recorded at a scan rate of 5 mV s^{-1}. The frequency range selected in the investigation of electrochemical impedance spectroscopy (EIS) was 100 kHz to 0.1 Hz. The turnover frequency (TOF) was evaluated as reported previously.[31–33]

$$E_{RHE} = E_{Ag/AgCl} + 0.197 + 0.059 \times iR.$$

Results and discussion

Hexagonal hematite (α-Fe₂O₃) nanorings (NRs) was prepared by a conventional hydrothermal method.[34] Fig. 1a shows XRD pattern of both α-Fe₂O₃ and bulk one, where all the diffraction peaks correspond to the α-Fe₂O₃ (PDF no. 72-0467). Further, SEM and TEM were performed to investigate structure and morphology of those samples, where the results indicate that α-Fe₂O₃ presents homogeneous NRs morphology (Fig. 1b, S1 and S2, ESI†). The length and ring diameter of α-Fe₂O₃ NRs are 39 nm and 28 nm, respectively (Fig. S3a and b, ESI†). High-
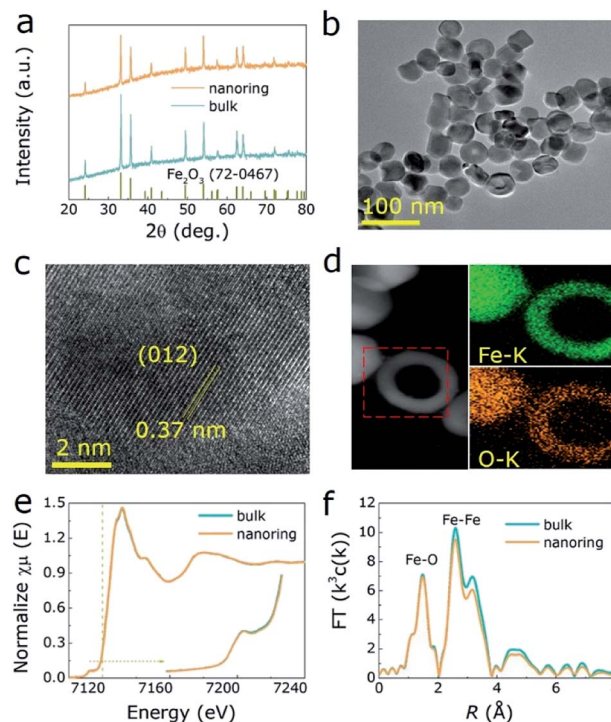

Fig. 1 (a) The XRD pattern of samples. The TEM (b), HRTEM (c) and EDX mapping images (d) of α-Fe₂O₃ NRs. The XANES spectra (e) and corresponding FT EXAFS (f) of Fe K-edge for two samples.

resolution TEM (HRTEM) image shows that α-Fe₂O₃ NRs have clear lattice spacing (0.37 nm, 0.27 nm, 0.25 nm and 0.14 nm) matches well with the (012), (104), (110) and (300) planes, respectively (Fig. 1c and S4, ESI†). Meanwhile, Fe and O elements are uniform distributed in α-Fe₂O₃ NRs matrix, as illustrated in energy dispersive X-ray (EDX) mapping images (Fig. 1d). To further investigate the change in electronic structure and coordination environment of Fe atoms in both samples, Fe K-edge XANES and EXAFS were measured. As shown in Fig. 1e, especially for the pre-edge peak, the intensity of α-Fe₂O₃ NRs is significantly reduced compared to the bulk one, confirming the higher local O coordination of the Fe atoms for α-Fe₂O₃ NRs.[35,36] Fig. 1f further displays the corresponding Fourier transforms (FT) of Fe K-edge EXAFS for two samples, where the peaks at 1.4 Å, 2.5 Å, 3.2 Å and 4.7 Å are attributed to the Fe–O, Fe–Fe, Fe–O/Fe coordination in α-Fe₂O₃ NRs.[37] It is of interest that the α-Fe₂O₃ NRs presents lower intensity than those of bulk ones, revealing the surface distortion and decreased structural homogeneity of bulk α-Fe₂O₃, corresponding to the results of wavelet transform (WT) simulation with the weaker central intensities for α-Fe₂O₃ NRs (Fig. S5 and Table S1, ESI†).

Besides, Fig. 2a presents the XPS results of Fe 2p spectrum, where the main peaks (726.4 eV, 712.4 eV) are 2p$_{1/2}$ and 2p$_{3/2}$ of Fe^{3+}, respectively. Besides, the minor peaks (723.8 eV, 710.2 eV) are Fe^{2+},[36] revealing there are some structural dislocation of the α-Fe₂O₃ NRs surface. For the O 1s result (Fig. 2b), the three peaks (O₁, O₂, O₃) correspond to surface adsorbed oxygen, oxygen vacancy and metal–oxygen peaks, respectively, where the
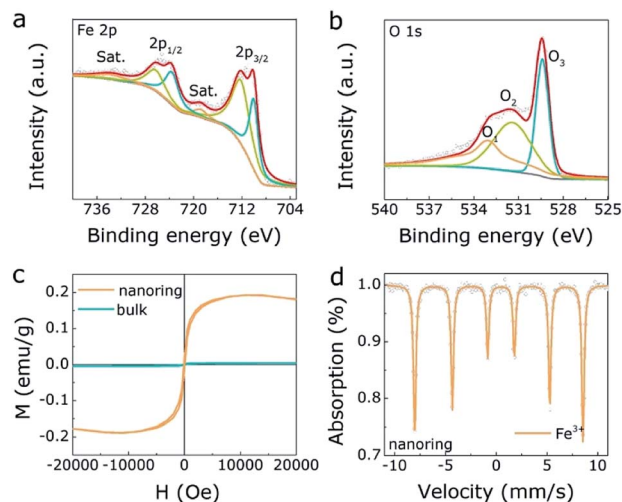
Fig. 2 The XPS spectrum of Fe 2p (a) and O 1s (b) for α-Fe$_2$O$_3$ NRs. (c) The magnetization hysteresis loops of α-Fe$_2$O$_3$ NRs and one. (d) The Mössbauer spectrum of α-Fe$_2$O$_3$ NRs.

appearance of oxygen vacancy gives rise to the structural dislocation of the α-Fe$_2$O$_3$ NRs surface. Meanwhile, there is no oxygen vacancy in bulk α-Fe$_2$O$_3$ sample (Fig. S6, ESI†). Furthermore, $M(H)$ hysteresis loops of the α-Fe$_2$O$_3$ NRs and bulk α-Fe$_2$O$_3$ were measured at room temperature to evaluate the magnetic property. As displayed in Fig. 2c, α-Fe$_2$O$_3$ NRs owns the saturation magnetization (M_s) of 0.19 emu g^{-1} and the coercivity (H_c) of 90 Oe, indicating the unique ferromagnetic interaction in α-Fe$_2$O$_3$ NRs. On the contrary, the bulk α-Fe$_2$O$_3$ exhibits antiferromagnetic property. These results reflect a magnetic transition of the α-Fe$_2$O$_3$ from antiferromagnetic to ferromagnetic nature, which mainly ascribed to the structural dislocation of the α-Fe$_2$O$_3$ NRs surface, in agreement with the XPS results. Mössbauer spectra and related parameters (Table S2, ESI†) were also investigated to confirm Fe valence states of both α-Fe$_2$O$_3$ NRs and bulk one. As displayed in the Fig. 2d and S7 (ESI),† the fitting results demonstrate that the dominated valence state is Fe^{3+} in both α-Fe$_2$O$_3$ NRs and bulk one.

The OER activities of α-Fe$_2$O$_3$ NRs, bulk α-Fe$_2$O$_3$ and Ir/C under acidic media (1 M HCl) were investigated by three-electrode device. Linear voltammetry scanning (LSV) curves of all electrocatalysts as exhibited in Fig. 3a and S8 (ESI†), where α-Fe$_2$O$_3$ NRs shows predominant OER performances with lower overpotential (1.43 V) than Ir/C (1.48 V) and bulk α-Fe$_2$O$_3$ (1.89 V) at 10 mA cm^{-2}, also the influence of electrocatalyst free substrate has been eliminated (Fig. S9, ESI†). Correspondingly, the Tafel slope values of α-Fe$_2$O$_3$ NRs, Ir/C, and bulk α-Fe$_2$O$_3$ are 138 mV dec^{-1}, 150 mV dec^{-1}, and 350 mV dec^{-1}, respectively, demonstrating that the α-Fe$_2$O$_3$ NRs owns the excellent intrinsic OER activity (with the lowest Tafel slope value) in acidic solution (Table S3, ESI†). In addition, the α-Fe$_2$O$_3$ NRs exhibits increased electrical conductivity with smaller charge transfer resistance (R_{ct}, 96 ohm) than bulk one (282 ohm), as illustrated in Fig. 3c. Moreover, Fig. 3d show the double layer capacitance (C_{dl}) of electrocatalysts, which is examined to assess effective
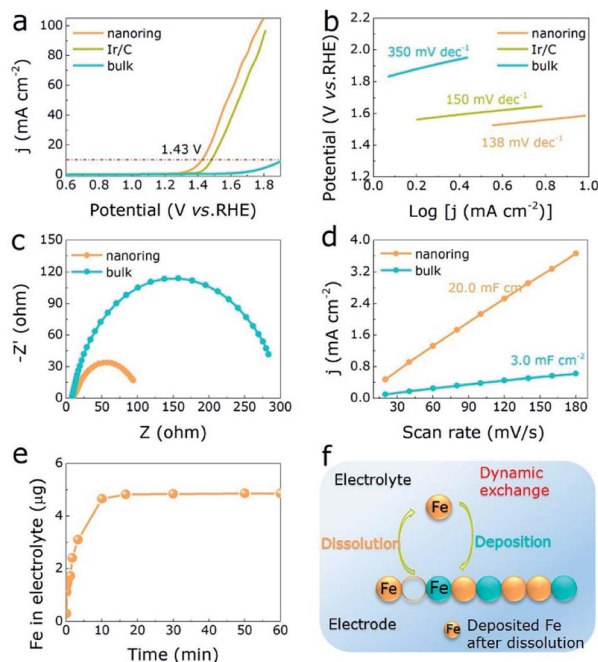

Fig. 3 (a) LSV curves and (b) Tafel slopes of α-Fe$_2$O$_3$ NRs, Ir/C and bulk one. (c) The EIS plots and C_{dl} curves (d) of both α-Fe$_2$O$_3$ electro-catalysts. (e) Fe dissolution of α-Fe$_2$O$_3$ NRs in the electrolyte with the beginning of OER CV cycling process (electrocatalysts supporting on glassy carbon electrode). (f) Schematic representation of α-Fe$_2$O$_3$ NRs dissolution during OER.

electrochemical active surface area (ECSA). The C_{dl} value of α-Fe$_2$O$_3$ NRs is about 7 times larger than that of the bulk one, indicating the α-Fe$_2$O$_3$ NRs electrocatalyst can expose more active sites for OER process. A larger TOF value of 2.3 O$_2$ s^{-1} at 1.7 V is obtained for the α-Fe$_2$O$_3$ NRs, compared to 1.3 O$_2$ s^{-1} for bulk one (Fig. S10a, ESI†), demonstrating the nanoring morphology has a great influence on the OER performances in α-Fe$_2$O$_3$. Distinctly, a rapid dissolution reaction of the α-Fe$_2$O$_3$ NRs occurs at the beginning of OER process under acidic condition, as displayed in the inductively coupled plasma mass spectrometry (ICP-MS) analyses (Fig. 3e), indicating that Fe atoms on the electrode surface are dynamic. It is of interest that after cyclic voltammetry (CV) cycling of 16.6 min, this dissolution rate reaches its maximum and keeps stable (4.8 μg), corresponding to the excellent OER activities as described above, demonstrating the formation of prominent α-Fe$_2$O$_3$ NRs electrocatalyst with high activity and dynamic stability (Fig. 3f). In addition, chronoamperometric response and CV cycling test display that the current loss and overpotential increase negligibly after 22 h continuous operation (Fig. 4a, S10b and c, ESI†), further demonstrating the superior OER stability under acidic condition. Both XRD pattern, TEM image, XPS spectra of Fe 2p, XANES and FT of Fe K-edge EXAFS of α-Fe$_2$O$_3$ NRs after long-time stability test shown in Fig. 4b–d, further exhibit well-retained crystallinity and electrocatalytic durability. These analyses confirm that the low-cost α-Fe$_2$O$_3$ NRs can effectively optimize the OER in acidic medium.
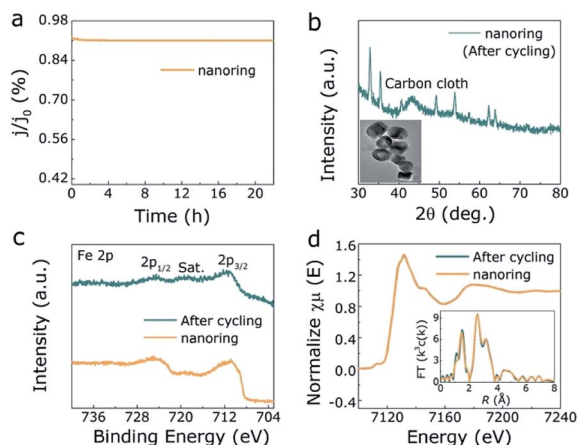
Fig. 4 (a) OER durability evaluation of α-Fe_2O_3 NRs electrocatalyst though chronoamperometric response. (b) XRD result (inset: TEM image) of α-Fe_2O_3 NRs after OER stability test. (c) Fe 2p spectra and (d) XANES spectra and EXAFS spectra of Fe K-edge in R-space (inset) of α-Fe_2O_3 NRs before and after OER cycling test.

Conclusions

In summary, we developed uniform α-Fe_2O_3 NRs as efficient OER electrocatalyst in acidic conditions with lower over-potential and robust durability. The promoted performance is mainly caused by the unique nanoring structure and disordered surface, which accelerates electron transfer, offers a large active surface area and great electrical conductivity (based on Tafel slope, C_{dl} and EIS results), giving rise to the boosted intrinsic electrocatalytic activity. This realizable finding provides a facile strategy to explore new hematite-based electrocatalysts with excellent performance and great stability for portable energy storage and conversion system.

Conflicts of interest

There are no conflicts of interest to declare.

Acknowledgements

Notes and references

1 L. C. Seitz, C. F. Dickens, K. Nishio, Y. Hikita, J. Montoya, A. Doyle, C. Kirk, A. Vojvodic, H. Y. Hwang and J. K. Norskov, *Science*, 2016, **353**, 1011–1014.

2 M. Q. Yang, J. Wang, H. Wu and G. W. Ho, *Small*, 2018, 1703323.

3 H. Wu, J. Geng, H. Ge, Z. Guo, Y. Wang and G. Zheng, *Adv. Energy Mater.*, 2016, **6**, 1600794.

4 C. Tang, H. S. Wang, H. F. Wang, Q. Zhang, G. L. Tian, J. Q. Nie and F. Wei, *Adv. Mater.*, 2015, **27**, 4516–4522.

5 C. C. L. Mccrory, S. Jung, I. M. Ferrer, S. M. Chatman and T. F. Jaramillo, *J. Am. Chem. Soc.*, 2015, **137**, 4347.

6 Y. Matsumoto and E. Sato, *Mater. Chem. Phys.*, 1986, **14**, 397–426.

7 C. C. L. Mccrory, S. Jung, J. C. Peters and T. F. Jaramillo, *J. Am. Chem. Soc.*, 2013, **135**, 16977–16987.

8 Z. F. Huang, J. J. Song, Y. H. Du and S. B. Xi, *Nat. Energy*, 2019, **4**, 329–338.

9 F. Dionigi and P. Strasser, *Adv. Energy Mater.*, 2016, 1600621.

10 C. Roy, B. Sebok, S. B. Scott and E. M. Fiordaliso, *Nat. Catal.*, 2018, **1**, 820–829.

11 L. Trotochaud, S. L. Young, J. K. Ranney and S. W. Boettcher, *J. Am. Chem. Soc.*, 2014, **136**, 6744–6753.

12 P. Zhou, Y. Wang, C. Xie, C. Chen, H. Liu, R. Chen, J. Huo and S. Wang, *Chem. Commun.*, 2017, **53**, 11778–11781.

13 F. L. Meng, G. Yilmaz, T. P. Ding, M. Gao and G. W. Ho, *Adv. Mater.*, 2019, **31**, 1903605.

14 D. A. Nedosekin, S. Ayyadevara, R. J. S. Reis, E. I. Galanzha and V. P. Zharov, *Proc. Natl. Acad. Sci. U. S. A.*, 2007, **104**, 20142.

15 T. Odedairo, X. C. Yan, X. D. Yao, K. Ken Ostrikov and Z. H. Zhu, *Adv. Mater.*, 2017, 1703792.

16 S. Yin, X. Ma and D. E. Ellis, *Surf. Sci.*, 2007, **601**, 2426–2437.

17 S. Yamamoto, T. Kendelewicz, J. T. Newberg, G. Ketteler and A. Nilsson, *J. Phys. Chem. C*, 2010, **114**, 2256–2266.

18 B. Klahr, S. Gimenez, F. Fabregat-Santiago, T. Hamann and J. Bisquert, *J. Am. Chem. Soc.*, 2012, **134**, 4294–4302.

19 J. Ahmed, T. Ahamad, N. Alhokbany, B. M. Almaswari, T. Ahmad, A. Hussain, E. S. S. Al-Farraj and S. M. Alshehri, *ChemElectroChem*, 2018, **5**, 3938–3945.

20 J. Ahmed, T. Ahamad, M. Ubaidullah, A. M. Al-Enizi and S. M. Alshehri, *Mater. Lett.*, 2018, **240**, 51–54.

21 S. M. Alshehri, J. Ahmed, T. Ahamad, P. Arunachalam, T. Ahmad and A. Khan, *RSC Adv.*, 2017, **7**, 45615–45623.

22 C. Yilmaz, C. F. Tan, Y. F. Lim and C. W. Ho, *Adv. Energy Mater.*, 2019, **9**, 1802981–1802983.

23 Q. Hu, G. Li, G. Li, X. Liu, B. Zhu, X. Chai, Q. Zhang, J. Liu and C. He, *Adv. Energy Mater.*, 2019, **9**, 1803861–1803867.

24 N. Danilovic, R. Subbaraman, K. C. Chang, S. H. Chang, Y. J. Kang, J. Snyder, A. P. Paulikas, D. Strmcnik, Y. T. Kim and D. Myers, *J. Phys. Chem. Lett.*, 2014, **5**, 2474–2478.

25 S. H. Chang, N. Danilovic, K. C. Chang, R. Subbaraman, A. P. Paulikas, D. D. Fong, M. J. Highland, P. M. Baldo, V. R. Stamenkovic and J. W. Freeland, *Nat. Commun.*, 2014, **5**, 4191.

26 N. Danilovic, R. Subbaraman, K. C. Chang and S. H. Chang, *Angew. Chem., Int. Ed. Engl.*, 2014, **53**, 14016–14021.

27 T. Binninger, R. Mohamed, K. Waltar, E. Fabbri, P. Levecque, R. Kötz and T. J. Schmidt, *Sci. Rep.*, 2015, **5**, 12167.

28 M. Huynh, T. Ozel, C. Liu, E. C. Lau and D. G. Nocera, *Chem. Sci.*, 2017, **8**, 4779–4794.

29 P. Strasser, *Adv. Energy Mater.*, 2016, **7**, 1601275.

30 J. S. Mondschein, J. F. Callejas, C. G. Read, J. Y. C. Chen, C. F. Holder, C. K. Badding and R. E. Schaak, *Chem. Mater.*, 2017, **29**, 950–957.

31 J. M. Qian, T. T. Wang and D. Q. Gao, *Appl. Catal., B*, 2019, **250**, 71–77.

32 L. Zhuang, L. Ge, Y. Yang, M. Li, Y. Jia, X. Yao and Z. Zhu, *Adv. Mater.*, 2017, **29**, 1606791–1606793.

33 P. T. Liu, J. Q. Ran, B. R. Xia, S. B. Xi and J. Wang, *Nano-Micro Lett.*, 2020, **12**, 1–12.

34 X. L. Liu, Y. Yang, C. T. Ng, L. Y. Zhao, Y. Zhang, B. H. Bay, H. M. Fan and J. Ding, *Adv. Mater.*, 2015, **27**, 1939–1944.

35 B. Zhang, X. Zheng, O. Voznyy, R. Comin, M. Bajdich, M. Garcia-Melchor, L. Han, J. Xu, M. Liu and L. Zheng, *Science*, 2016, **352**, 333–337.

36 H. Wu, T. Yang, Y. H. Hua and G. W. Ho, *Adv. Mater.*, 2018, **30**, 1804341.

37 W. R. Cheng, J. F. He and S. Q. Wei, *J. Am. Chem. Soc.*, 2014, **136**, 10393–10398.